Progress In Electromagnetics Research C, Vol. 111, 1–14, 2021

Investigating the Performance of a New Type of Preloaded Linear Stroke Length Magnetic Spring

Hossein Baninajar, Jonathan Z. Bird*, and Victor Albarran

Abstract—This paper presents the analytic analysis and proof-of-principle prototyping of a new type of magnetic spring with preload and a linear stroke length. An analytic based magnetic charge modeling approach is utilized to investigate design rules that can maximize the magnetic spring's energy density, stiffness characteristics, and linearity. It is shown that whilst the proposed magnetic spring has a lower mass and energy density than a mechanical spring, the magnetic spring offers several unique characteristics, such as contact-free operation, inherent preload, as well as over-force failure protection. In addition, the operating principle of the presented magnetic spring can be extended to realize both positive and negative variable stiffness adjustment characteristics.

1. INTRODUCTION

Magnetic springs are being researched for use in vibration isolators [1–14], energy scavenging devices [15–17], robot actuators [18], as well as permanent magnet bearings [19–22]. All of the magnet springs that have been studied to-date appear to operate by using the north-south repulsion between vertical magnets [3–8, 17, 18] or horizontally positioned magnets [1–3, 9, 11, 18, 21]. Both approaches often have a limited stroke length, and the force relationship is normally non-linear. Hol [1] investigated the vibration isolation magnet arrangement as shown in Figure 1(a). In this arrangement, the central magnet is unstable when being centered [7, 12, 13, 22], but as the side magnets are longer than the center magnet, a surprisingly constant force can be created, and this force relationship is shown in Figure 2(a). If the central magnet is made to be the same length as the side magnet, as shown in Figure 1(b), then a remarkably linear force relationship can be created, as illustrated in Figure 2(b). A change in stiffness can then be created by shifting opposing magnets along the y-axis, as shown in Figure 3.

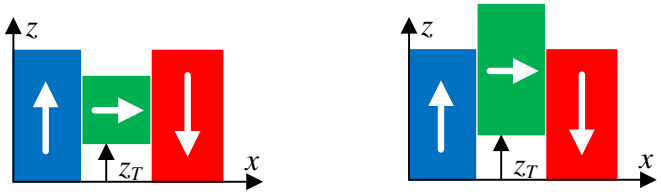

Figure 1. (a) The constant force magnet spring arrangements studied by (a) Hol [1] and (b) the constant stiffness magnet spring arrangement studied in this paper.

Received 15 January 2021, Accepted 3 March 2021, Scheduled 11 March 2021
* Corresponding author: Jonathan Bird (jonathan.bird@ieee.org).
The authors are with the Laboratory for Magnetomechancial Energy Conversion and Control, Department of Electrical and Computer Engineering, Portland State University, Portland, OR, USA.

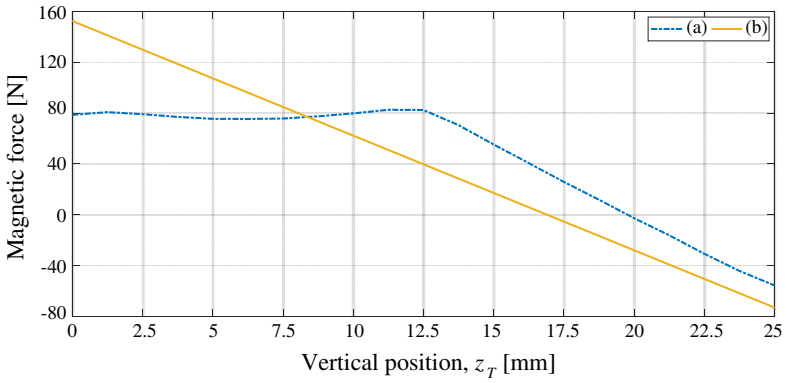

Figure 2. 2-D finite element analysis calculated magnetic force comparison between the constant force and constant stiffness magnetic spring arrangements shown in Figure 1.

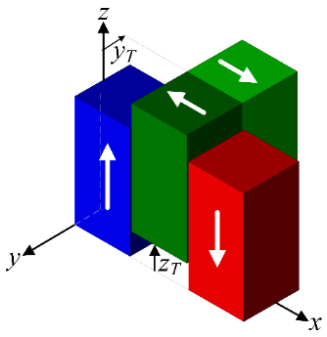

Figure 3. Magnetic spring with an adjustable stiffness capability. When the green magnets are shifted along the y-axis the spring stiffness can be changed.

This paper's research contribution relates to studying the energy density and linearity characteristics of the pre-loaded magnet spring arrangement shown in Figure 1(b). The force, linearity, and energy density are studied using a 3-D analytic-based model, and the energy density of the magnetic spring is compared to an equivalent mechanical spring. The magnet arrangement shown in Figure 1(b) is indeed simple in form and forms a single pole-pair segment of a Halbach magnet array [25]. Despite its simplicity, the authors have been unable to locate any other authors that have studied its unique linear force-displacement stroke length characteristics.

2. FIELD, FORCE AND ENERGY DERIVATION

The geometry and coordinate axis for the cuboidal magnet arrangement being studied are shown in Figures 4(a)–(c). The magnetic flux density due to the rectangular cuboidal side magnets has been evaluated using the magnetic charge sheet modelling approach. Since the fields are antisymmetric with respect to the center (green) magnet, the field effect of only the left side (blue) magnet and center magnet needs to be evaluated. Using this symmetry allows the partial magnetic charge sheet model, as shown in Figure 4(c), to be used [23].

In the current-free region, the governing magnetostatic Maxwell's equations are

$$\nabla \times \mathbf{H} = 0 \tag{1}$$

$$\nabla \cdot \mathbf{B} = 0 \tag{2}$$

where $\mathbf{B}$ and $\mathbf{H}$ are magnetic flux density and field intensity, respectively. The magnetic flux density and field intensity are related by

$$\mathbf{B} = \mu_0 \mathbf{H} + \mu_0 \mathbf{M}(\mathbf{H}). \tag{3}$$

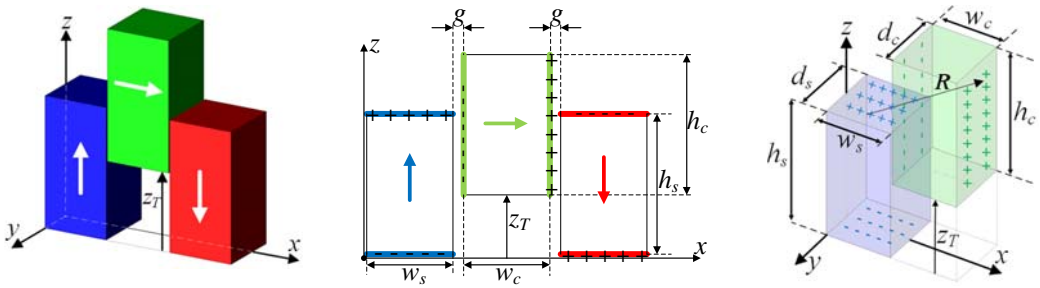

Figure 4. (a) A 3-D perspective model, the central magnet translates, and the side magnets are stationary, (b) and (c) shows the magnetic charge and geometric definitions.

where μ_0 = permeability of free space. The magnetization vector is a function of $\mathbf{H}$ and is defined by the magnetic constitutive equation [10, 13]

$$\mathbf{M}(\mathbf{H}) = \chi_m \mathbf{H} + \mathbf{M}_m \tag{4}$$

where χ_m = magnetic susceptibility. Substituting Eq. (4) into Eq. (3) gives:

$$\mathbf{B} = \mu_0 \mu_r \mathbf{H} + \mu_0 \mathbf{M}_m \tag{5}$$

where the relative permeability is

$$\mu_r = \chi_m + 1. \tag{6}$$

The magnetic scalar potential, ϕ, is related to the magnetic field intensity by [2]:

$$\mathbf{H} = -\nabla\phi. \tag{7}$$

Taking the divergence of both sides of Eq. (5) and substituting Eqs. (2) and (7) gives:

$$\nabla^2\phi = \frac{\nabla \cdot \mathbf{M}_m}{\mu_r}. \tag{8}$$

Only the field emanating from the side magnets needs to be evaluated. The magnetization vector, $\mathbf{M_m}$, is uniform within the magnet volume, so the divergence of $\mathbf{M}_m$ is only non-zero on the permanent magnet boundaries. Using the coordinate (x_o, y_o, z_o) to define the surface location on the side magnet the magnetization vector $\mathbf{M_m}$ is directed inwards and outwards at $z_o = 0$ and $z_o = h_s$ such that

$$\mathbf{M}_m(x_o, y_o, h_s) = \sigma_{sm}\widehat{\mathbf{z}} \tag{9}$$

$$\mathbf{M}_m(x_o, y_o, 0) = -\sigma_{sm}\widehat{\mathbf{z}} \tag{10}$$

where

$$\sigma_{sm} = B_r/\mu_0. \tag{11}$$

is the magnetic surface charge density and B_r = permanent magnet remnant flux density. The charge value on the side magnet is only non-zero at the top and bottom surfaces of the side magnet, as shown in Figures 4(b) and (c). Using the coordinate definition shown in Figure 4(c), Equation (8) was evaluated using an integral solution approach [10, 24]. The stationary left side magnet (shown in blue) was evaluated, this gives

$$\phi(x, y, z) = \phi_s(x, y, z, h_s) - \phi_s(x, y, z, 0) \tag{12}$$

where [10, 24]

$$\phi_s(x, y, z, z_o) = \frac{\sigma_{sm}}{4\pi\mu_r} \int_0^{w_s} \int_{-d_s/2}^{d_s/2} \frac{1}{R(x, y, z, x_o, y_o, z_o)} dy_o dx_o \tag{13}$$

and the vector length is

$$R(x, y, z, x_o, y_o, z_o) = \sqrt{(x - x_o)^2 + (y - y_o)^2 + (z - z_o)^2}. \tag{14}$$

The coordinate (x, y, z) is the observation point of interest. Due to symmetry the field intensity from the right-side magnet interacting with the central magnet will be the same as that of the left side magnet.

The central magnet magnetic charge density, σ_{cm}, is constant and located at $x = w_s + g$ and $x = w_s + w_c + g$, as shown in Figures 4(b) and (c). The central magnet can move along the z-axis and at a particular stroke position, z_T, the interaction energy, U, between the central magnet magnetic surface charge density, σ_{cm}, and the side magnets' scalar field, ϕ, is [25]

$$U(z_T) = U_s(z_T, w_s + w_c + g) - U_s(z_T, w_s + g) \tag{15}$$

where

$$U_s(z_T, x) = 2\mu_0\sigma_{cm} \int_{-d_c/2}^{d_c/2} \int_{z_T}^{h_c+z_T} \phi(x, y, z) dz dy \tag{16}$$

This interaction energy is analogous to the mutual inductance energy between windings. Like with mutual inductance energy the magnet interaction energy can have a positive or negative value. The force along the stroke length is computed from

$$\mathbf{F}(z_T) = -\nabla\, U(z_T)|_{\sigma_{cm}=\text{constant}}\,. \tag{17}$$

giving

$$\mathbf{F}(z_T) = \mathbf{F}_s(z_T, w_s + w_c + g) - \mathbf{F}_s(z_T, w_s + g) \tag{18}$$

where [26]

$$\mathbf{F}_s(z_T, x) = 2\mu_0\sigma_{cm} \int_{-d_c/2}^{d_c/2} \int_{z_T}^{h_c+z_T} \mathbf{H}(x, y, z) dz dy \tag{19}$$

Equation (18) provides insight by showing that the linearity of the force is dependent on the uniformity of the vertical H_z field:

$$F_z(z_T) = 2\mu_0\sigma_{cm} \int_{-d_c/2}^{d_c/2} \int_{z_T}^{h_c+z_T} [H_z(w_s + w_c + g, y, z) - H_z(w_s + g, y, z)] dz dy \tag{20}$$

Substituting Eq. (12) into Eq. (7), the H_z field intensity due to the left side magnet is

$$H_z(x, y, z) = H_s(x, y, z, h_s) - H_s(x, y, z, 0) \tag{21}$$

where

$$H_s(x, y, z, z_o) = \frac{\sigma_{sm}(z - z_o)}{4\pi\mu_r} \int_0^{w_s} \int_{-d_s/2}^{d_s/2} \frac{1}{R(x, y, z, x_o, y_o, z_o)^3} dy_o dx_o. \tag{22}$$

Evaluating Eq. (22) gives

$$H_s(x, y, z, z_o) = \frac{\sigma_{sm}}{4\pi\mu_r} \left[\Psi_z\left(w_s, \frac{d_s}{2}, z_o\right) - \Psi_z\left(w_s, -\frac{d_s}{2}, z_o\right) - \Psi_z\left(0, \frac{d_s}{2}, z_o\right) + \Psi_z\left(0, -\frac{d_s}{2}, z_o\right) \right] \tag{23}$$

where

$$\Psi_z(x_o, y_o, z_o) = \tan^{-1}\left(\frac{(x - x_o)(y - y_o)}{(z - z_o) R(x, y, z, x_o, y_o, z_o)} \right). \tag{24}$$

The double integral force equation was computed by using the MATLAB® function integral2.m with an absolute tolerance setting of 1×10^{-8}. Equation (20) will be used in the force and energy density analysis. It should be noted that the force can also be evaluated using the scalar potential. By substituting Eq. (12) into Eq. (15) and evaluating Eq. (17) yields

$$\begin{aligned} F_z(z_T) \;=\; & 2\mu_0\sigma_{cm} \int_{-d_c/2}^{d_c/2} [\phi(w_s + w_c + g, y, z_T) \\ & -\phi(w_s + w_c + g, y, h_c + z_T) + \phi(w_s + g, y, h_c + z_T) - \phi(w_s + g, y, z_T)] dy. \end{aligned} \tag{25}$$

This eliminates the need to evaluate the z-axis integral, but the double integral evaluation of the magnetic scalar potential is more challenging; therefore, Eq. (20) was used in the energy and linearity analysis.

3. FORCE AND ENERGY CHARACTERISTICS

The field and force equations were validated by using a 3-D magnetostatic finite element analysis (FEA) method and an experimental setup. Using the geometric and material properties defined in Table 1, the force and energy comparison between the analytic, 3-D FEA model and experimentally measurements are compared in Figure 5 and Figure 6. Figure 5 shows that the 3-D analytic-based model accurately predicts the force values, but the 3-D model is not as linear as the 2-D analysis predicted. The higher force value and the greater linearity shown by the 2-D analysis are due to neglecting the magnet width, thereby neglecting the y-axis flux leakage and edge effects. Figure 6 shows how the energy changes with force. The peak positive force is almost double the peak negative force. The maximum force position, at $z_T = 0$, has zero interaction energy. Figure 7 shows how the peak force changes as the magnet width increases, and the analytic model accurately predicts the parameter change. An experimental setup used to validate the model is shown in Figure 8.

Figure 9 shows the magnetic flux density comparison between the numerical and analytic models. It can be noted that the B_z field component is not constant along the stroke length, which results in the force not being fully linear. Section 4 discusses geometric parameters that improve the linearity.

Table 1. Geometric and material properties for the rectangular magnets.

Parameter		Value	Units
Side magnets	Height, h_s	25	mm
	Width, w_s	12.5	mm
	Depth, d_s	12.5	mm
Central magnet	Height, h_c	25	mm
	Width, w_c	12.5	mm
	Depth, d_c	12.5	mm
	Air-gap between magnets, g	0.35	mm
Magnet properties (Nd-Fe-B, N48)	Residual flux density, B_r	1.39	T
	relative permeability, μ_r	1.04	-
	Mass density	7500	kg/m^3

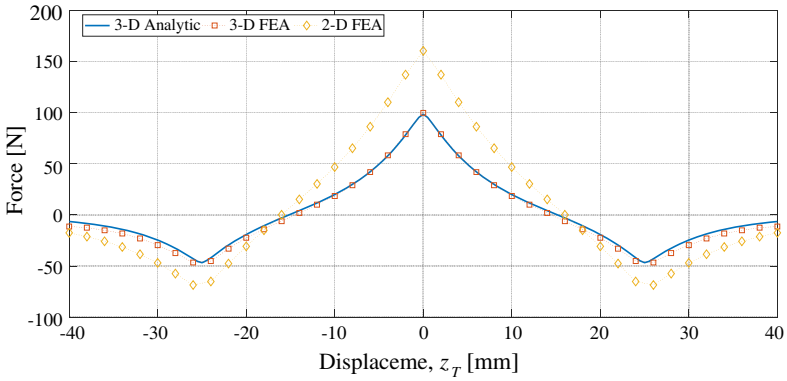

Figure 5. Analytic based magnetic charge model comparison with a 3-D and 2-D finite element analysis model.

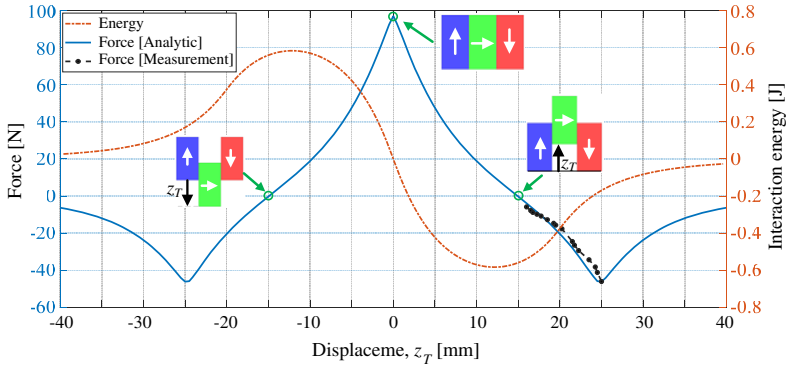

Figure 6. Force and interaction energy for the proof-of-principle magnetic spring. Also shown is (a) zero force positive stiffness (stable) magnet position, (b) maximum force magnet position and (c) zero force negative stiffness position.

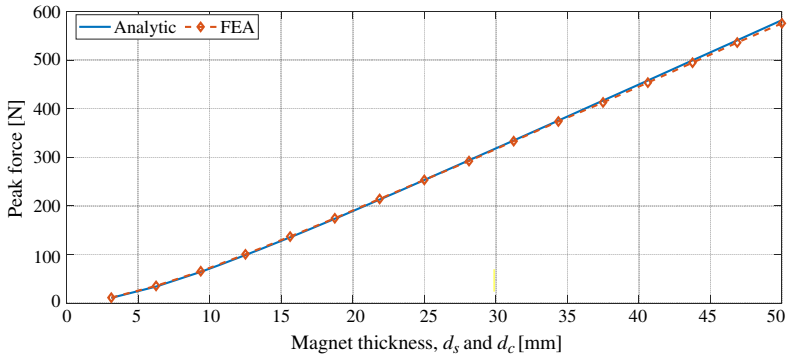

Figure 7. Peak magnetic force comparison between the analytic-based model and the FEA.

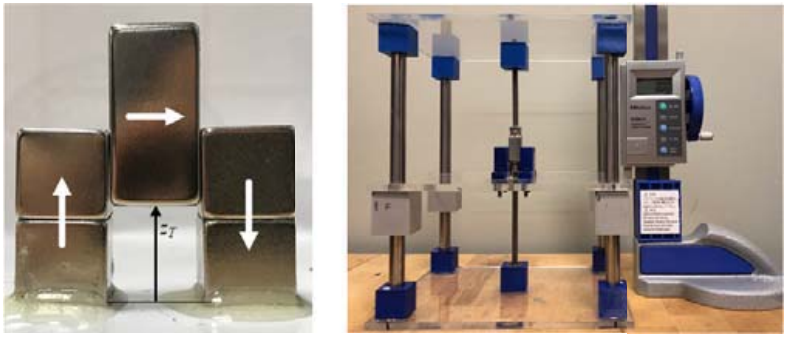

(a) (b)

Figure 8. (a) The simple magnetic spring used to validate the force equation and linearity characteristics. (b) The experimental setup used to measure the force and position. The setup measured the negative, z_T stroke length.

4. SCALING AND PERFORMANCE ANALYSIS

Using the presented analytic-based model, a scaling analysis was conducted to ascertain the linearity and energy density of the presented magnetic spring. The stroke length linearity was assessed by evaluating the coefficient of determinant, r^2 [27] for each geometric design. The r^2 value measures the distance between the force path and the fitted line. A path with perfect linearity has an r^2 value of unity. The

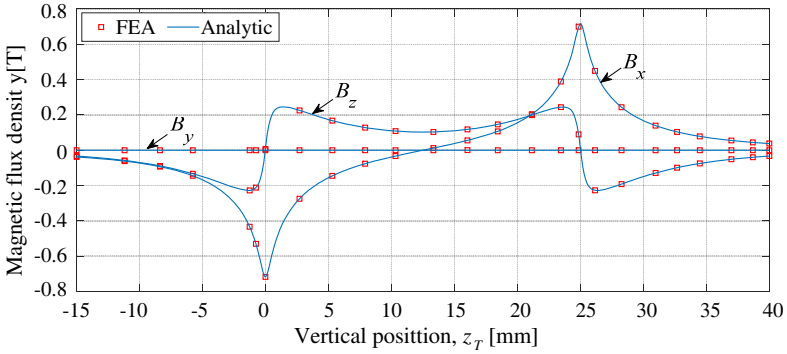

Figure 9. The analytic and 3-D finite element analysis field comparison due to both side magnets along the stroke length, z-axis, at $(x, y) = (25.35, 0)$ mm. The Appendix shows the analytic field solution for the B_x and B_y field components used in the Figure 9 plot.

energy was evaluated by computing the work done:

$$U(z_o) - U(0) = \int_0^{z_o} F_z\left(z_T\right) dz_T \tag{26}$$

where $z_T = z_o$ is the zero-force position. As the interaction potential energy is zero at $z_T = 0$, the energy density can be evaluated by using

$$U_{dm} = \frac{U(z_o)}{[2h_s w_s d_s + h_c d_c d_c]\rho_m} \tag{27}$$

The following height, h, width, w, and depth, d, magnet ratios were used in the scaling analysis:

$$\Gamma_h = \frac{h_s}{h_c}. \tag{28}$$

$$\Gamma_w = \frac{w_s}{w_c} \tag{29}$$

$$\Gamma_d = \frac{d_s}{d_c}. \tag{30}$$

where subscripts c and s denote center and side magnet lengths, respectively. A central magnet width-to-height ratio

$$\Gamma_{wh} = \frac{w_c}{h_c} \tag{31}$$

and central magnet depth-to-width ratio

$$\Gamma_{dw} = \frac{d_c}{w_c} \tag{32}$$

were also used. Using the ratio values defined in Table 2, the energy density and stroke linearity were evaluated for each geometric combination when the central magnet height was fixed at $h_c = 25$ mm, and the height ratio was fixed at $\Gamma_h = 1$. The height ratio was fixed because it allows an equivalent mechanical spring stroke length comparison to be made. Additionally, it was observed that the preload force and positive stroke length are maximum when $\Gamma_h = 1$. This can be seen by looking at Figure 10 in which the force and stroke length for different Γ_h values are shown.

The change in energy density, linearity, and force when using the geometric values shown in Table 2 is summarized in Figure 11. The maximum symmetrical force shown in Figure 11(b) is defined as

$$F_{z,sym} = F_z(0) - F_z(12.5) \tag{33}$$

The design with the largest peak force has the highest stiffness and linearity. When the force is below $F_{z,sym} = 690$ N, there is a trade-off between the energy density and linearity. By examining the energy density solutions, a number of geometric design rules can be determined. These design rules are discussed in the following sections.

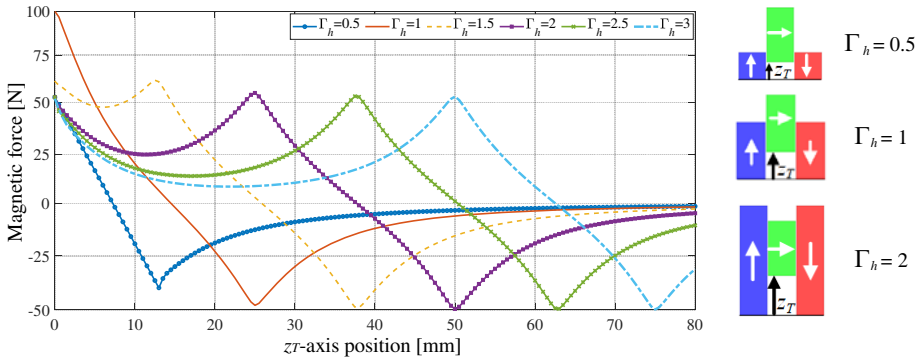

Figure 10. Magnetic force applied on the central magnet vs. stroke length displacement, z_T. The magnetic spring arrangements on the right correspond to the designs with $h_c = 25\,\text{mm}$ and $\Gamma_h = 0.5$, 1, and 2. The other ratios were fixed at $(\Gamma_w, \Gamma_d, \Gamma_{wh}, \Gamma_{dw}) = (1, 1, 0.5, 0.5)$.

Table 2. Magnet sweep parameters.

Geometric Parameter	Range
Central magnet height, h_c [mm]	25
Airgap length, g [mm]	0.35
Magnet height ratio, Γ_h	1
Magnet width ratio, Γ_w	$[0.2, 0.3, \ldots, 2]$
Magnet depth ratio, Γ_d	$[0.5, 0.75, \ldots, 2]$
Central magnet width-to-height ratio, Γ_{wh}	$[0.2, 0.3, \ldots, 2]$
Central magnet depth-to-width ratio, Γ_{dw}	$[0.25, 0.5, \ldots, 3]$

4.1. Depth-to-Width Ratio, Γ_{dw}

The energy density as a function of central magnet depth-to-width and width-to-height ratio is shown in Figure 12 for the case when $(\Gamma_h, \Gamma_w, \Gamma_d) = (1, 0.5, 1)$. The energy density increases, but with diminishing returns as the depth-to-width ratio, Γ_{dw}, increases. When $\Gamma_{dw} > 3$, the edge effects are minimal; the model approaches the ideal 2-D form; Γ_{dw} can be used to adjust the required force value. When $\Gamma_{dw} \geq 3$, a width-to-height ratio $\Gamma_{wh} = 1$ maximizes the energy density. To highlight how the other parameters affect each other's performance, $\Gamma_{dw} = 3$ is used in the remaining parameter discussion.

4.2. Depth Ratio, Γ_d and Width Ratio, Γ_w

Figure 13 shows how the energy density as a function of depth ratio, Γ_d, and width ratio, Γ_w, changes when $(\Gamma_h, \Gamma_{dw}) = (1, 3)$. The peak energy density occurs at $\Gamma_d = 1$ for all Γ_w values. In order to maximize the energy density

$$\frac{w_c}{2w_s} = \frac{d_s}{d_c} \tag{34}$$

must be satisfied. The designs that meet this criterion are on the Pareto front in Figure 11(b).

4.3. Width-to-Height Ratio, Γ_{wh}

When $(\Gamma_h, \Gamma_d, \Gamma_{dw}) = (1, 1, 3)$, Figure 14 shows how the energy density changes with the width ratio and central magnet's width-to-height ratio. The energy density is maximum when $(\Gamma_{wh}, \Gamma_w) = (1, 0.5)$.

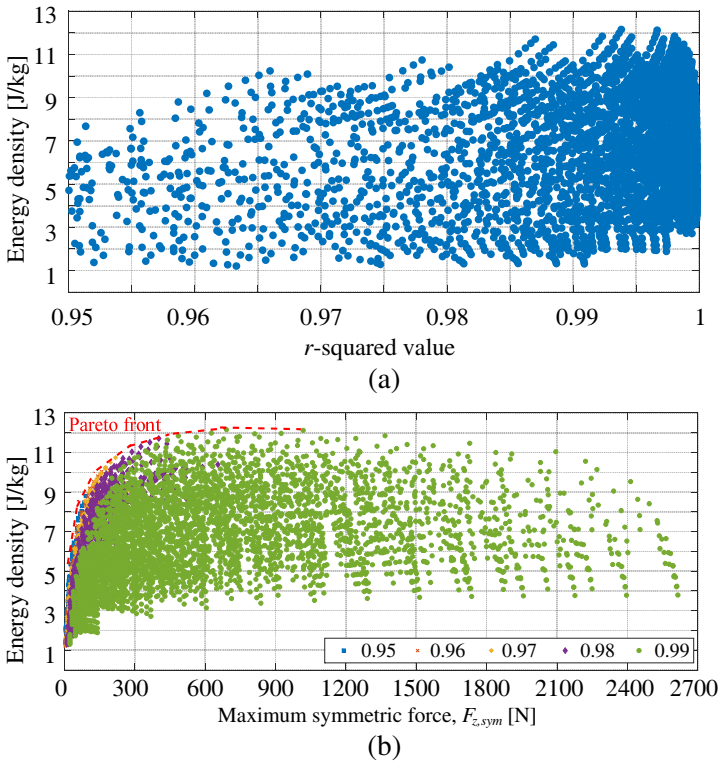

Figure 11. (a) Energy density versus linearity, r_2 value. (b) Energy density versus maximum symmetrical force value. The legend shows the r_2 value.

Table 3. Magnetic spring performance comparison.

Parameter		Initial (a)	Peak energy density (b)	Improved (c)	Units
Central magnet	Height, h_c	25	25	25	mm
	Width-to-height ratio, Γ_{wh}	0.5	1	1	-
	Depth-to-height ratio, Γ_{dw}	1	3	0.57	-
Side magnets	Height ratio, Γ_h	1	1	1	-
	Width ratio, Γ_w	1	0.5	0.5	-
	Depth ratio, Γ_d	1	1	1	-
Peak force		98.5	1,118.3	127.2	N
Peak symetrical force		56.5	690.9	74.4	N
Pre-load force		9.7	225.7	15.0	N
Mass		87	702.3	132.7	g
Stiffness constant		5.17	62.4	6.83	kN/m
Mass energy density		6.64	12.15	7.01	J/kg
Volume energy density		43.7	74.5	44.6	kJ/m^3
Coefficient of determinant, r^2 value		0.96	0.99	0.97	-

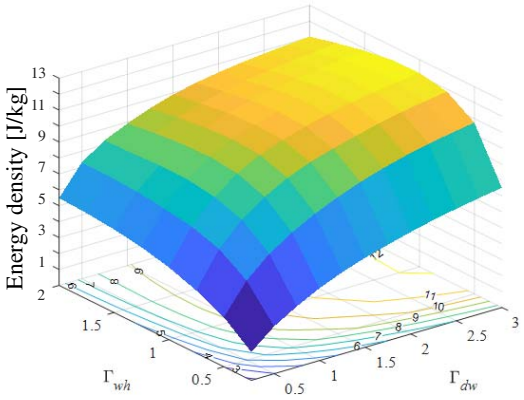

Figure 12. Energy density change when the width-to-height and depth-to-width ratio are varied. This is for the case when $(\Gamma_h, \Gamma_w, \Gamma_d) = (1, 0.5, 1)$.

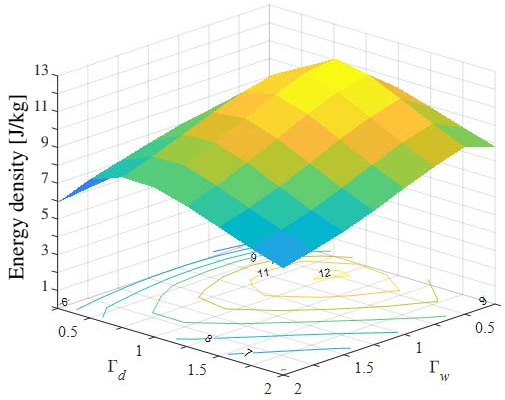

Figure 13. Energy density as a function of magnet width ratio, Γ_w, and depth ratio, Γ_d.

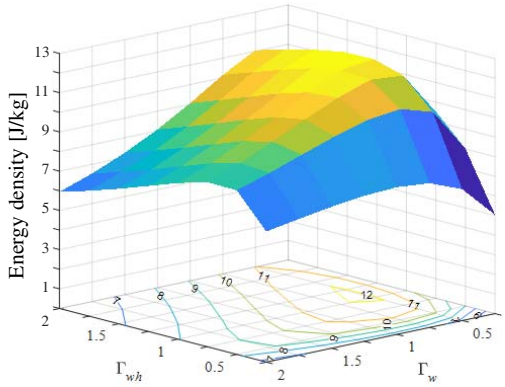

Figure 14. Energy density as a function of the central magnet's width-to-height ratio, Γ_{wh}, and width ratio Γ_w.

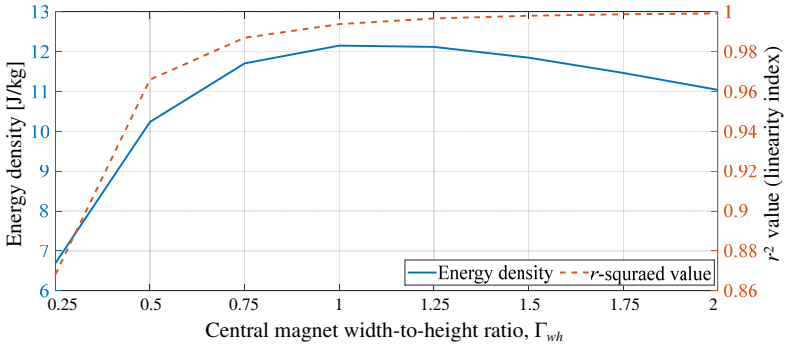

Figure 15. Shows how the linearity, measured using the r^2 value improves when the width-to-height ratio, Γ_{wh}, increases. The energy density is maximum when $\Gamma_{wh} = 1$.

However, Figure 15 shows that the linearity keeps improving beyond $\Gamma_{wh} = 1$. The improving linearity with increased Γ_{wh} is because when Γ_{wh} increases the B_z magnetic flux density becomes more uniform along the stoke length; this is shown in Figure 16.

Table 3(a) shows the initial proof-of-principle design values. Table 3(b) shows the values that yield the peak energy density for a 12.5 mm stroke length, and this peak energy density uses all the design

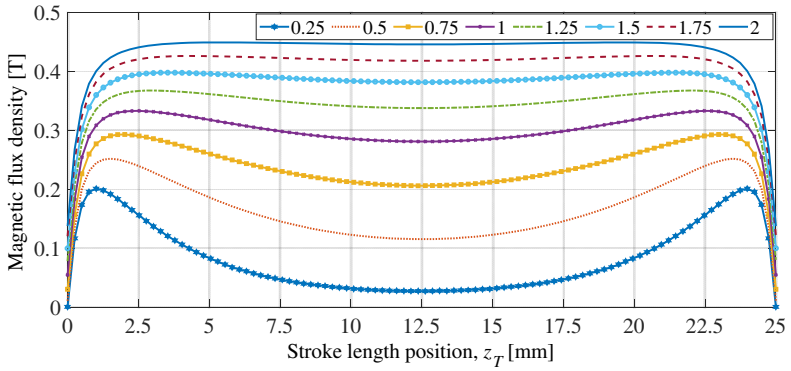

Figure 16. Magnetic flux density B_z along the stroke length at $(x,y) = (w_s + g + w_c, 0)$ when $(\Gamma_{dw}, \Gamma_w, \Gamma_d) = (3, 0.5, 1)$. The legend shows the different central magnet width-to-height ratios.

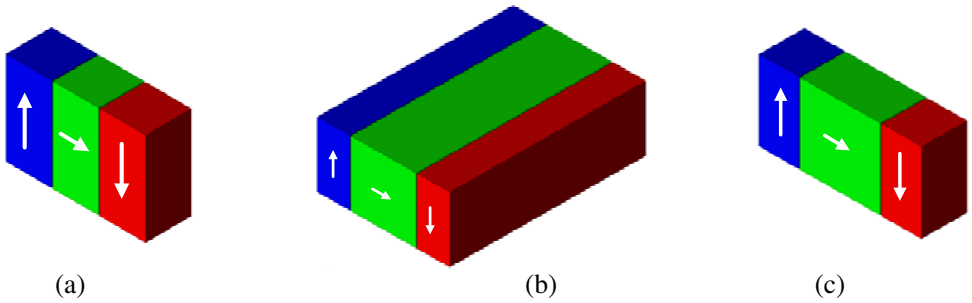

Figure 17. (a) Initial design, (b) peak energy density design, and (c) improved initial design.

Table 4. Mechanical spring performance comparison.

Mechanical Spring Characterstic	High Force [28]	Low Force [29]	Units
Peak force	1120	127.3	N
Outer diameter	30.9	34.2	mm
Length (unloaded)	76.2	25.4	mm
Mass	200.1	14.0	g
Stroke length	12.45	12.55	mm
Stiffness constant	90.0	10.1	kN/m
Mass energy density	34.9	57.0	J/kg
Volume energy density	118.3	82.6	kJ/m^3

specifications outlined above. The peak force and energy density are then 1,118 N and 12.15 J/kg, respectively. The peak energy density design has a large force because the width is larger, as shown in Figure 17. Table 3(c) shows a design that improves on the linearity and energy density of the initial design without greatly increasing the force.

Table 4 shows the performance of mechanical spring designs that have a comparable stroke length and force value. One can note that the mechanical spring's mass and volumetric energy density is significantly higher, 3 times and 1.6 times smaller in mass and volume.

5. CONCLUSION

This paper presented an analytic design, analysis, and proof-of-principle prototype of a new type of linear stroke length compression magnetic spring with pre-load. An analytic based magnetic charge modeling approach was used to investigate the magnetic spring energy density and linearity in order to approximately compare the magnetic springs performance with equivalently sized mechanical springs. Magnetic spring sizing design rules were also suggested, whilst it was shown that the energy density of the magnetic spring is significantly lower than a comparable mechanical spring. The magnetic spring offers a number of unique characteristics, such as contact free operation, inherent preload, over-force failure protection, as well as the ability to use designs that enable stiffness adjustment to be achieved.

ACKNOWLEDGMENT

The authors would like to thank the JMAG Corporation for the use of their FEA software. This material is based upon work partially supported by the Department of Energy's Office of Energy Efficiency and Renewable Energy (EERE) under the Water Power Technologies Office award number DE-EE0001837.

APPENDIX A.

The magnetic field intensity, H_x and H_y as shown in Figure 9, was calculated by evaluating the field contribution from the left and right side magnets and then adding the result. For example, the field from the left side magnet is given by:

$$H_x(x,y,z) \;=\; H_{sx}(x,y,z,h_s) - H_{sx}(x,y,z,0) \tag{A1}$$

$$H_y(x,y,z) \;=\; H_{sy}(x,y,z,h_s) - H_{sy}(x,y,z,0) \tag{A2}$$

where

$$H_{sx}(x,y,z,z_o) \;=\; \frac{\sigma_{sm}}{4\pi\mu_r}\int_0^{w_s}\int_{-d_s/2}^{d_s/2}\frac{(x-x_o)}{R(x,y,z,x_o,y_o,z_o)^3}dy_o dx_o \tag{A3}$$

$$H_{sy}(x,y,z,z_o) \;=\; \frac{\sigma_{sm}}{4\pi\mu_r}\int_0^{w_s}\int_{-d_s/2}^{d_s/2}\frac{(y-y_o)}{R(x,y,z,x_o,y_o,z_o)^3}dy_o dx_o \tag{A4}$$

Evaluating Eq. (A3) gives

$$H_{sx}(x,y,z,z_o) = \frac{\sigma_{sm}}{4\pi\mu_r}\left[\Psi_x\left(w_s,\frac{d_s}{2},z_o\right) - \Psi_x\left(w_s,-\frac{d_s}{2},z_o\right) - \Psi_x\left(0,\frac{d_s}{2},z_o\right) + \Psi_x\left(0,-\frac{d_s}{2},z_o\right)\right] \tag{A5}$$

where

$$\Psi_x(x_o,y_o,z_o) = \ln\sqrt{(y-y_o)+R(x,y,z,x_o,y_o,z_o)}. \tag{A6}$$

And evaluating Eq. (A4) gives

$$H_{sy}(x,y,z,z_o) = \frac{\sigma_{sm}}{4\pi\mu_r}\left[\Psi_y\left(w_s,\frac{d_s}{2},z_o\right) - \Psi_y\left(w_s,-\frac{d_s}{2},z_o\right) - \Psi_y\left(0,\frac{d_s}{2},z_o\right) + \Psi_y\left(0,-\frac{d_s}{2},z_o\right)\right] \tag{A7}$$

where

$$\Psi_y(x_o,y_o,z_o) = \tanh^{-1}\left(\frac{R(x,y,z,x_o,y_o,z_o)}{(x-x_o)}\right). \tag{A8}$$

REFERENCES

1. Hol, S. A. J., "Design and optimization of a magnetic gravity compensator," Ph.D. Dissertation, Eindhoven University of Technology, 2004.
2. Patt, P. J., M. Kisco, and F. R. Stolfi, "Linear magnetic spring and spring/motor combination," Patent 5,017,819, 1989.
3. Robertson, W., B. Cazzolato, and A. Zander, "A multipole array magnetic spring," *IEEE Transactions on Magnetics*, Vol. 41, No. 10, 3826–3828, 2005, doi: 10.1109/TMAG.2005.854981.
4. Robertson, W., "Modelling and design of magnetic levitation systems for vibration isolation," Thesis, 2013.
5. Wu, W., X. Chen, and Y. Shan, "Analysis and experiment of a vibration isolator using a novel magnetic spring with negative stiffness," *Journal of Sound and Vibration*, Vol. 333, No. 13, 2958–2970, Jun. 23, 2014, doi: https://doi.org/10.1016/j.jsv.2014.02.009.
6. Casteren, D. T. E. H. V., J. J. H. Paulides, J. L. G. Janssen, and E. A. Lomonova, "Analytical force, stiffness, and resonance frequency calculations of a magnetic vibration isolator for a microbalance," *IEEE Transactions on Industry Applications*, Vol. 51, No. 1, 204–210, 2015, doi: 10.1109/TIA.2014.2328780.
7. Zhang, H., B. Kou, Y. Jin, and H. Zhang, "Modeling and analysis of a new cylindrical magnetic levitation gravity compensator with low stiffness for the 6-DOF fine stage," *IEEE Transactions on Industrial Electronics*, Vol. 62, No. 6, 3629–3639, 2015, doi: 10.1109/TIE.2014.2365754.
8. Olaru, R., A. Arcire, C. Petrescu, M. M. Mihai, and B. Gîrtan, "A novel vibration actuator based on active magnetic spring," *Sensors and Actuators A: Physical*, Vol. 264, 11–17, Sep. 01, 2017, doi: https://doi.org/10.1016/j.sna.2017.07.041.
9. Paden, B. E., C. Chen, and O. J. Fiske, "Magnetic spring and actuators with multiple equilibrium position," Patent 7,265,470 B1, 2009.
10. Janssen, J., "Extended analytical charge modeling for permanent-magnet based devices: Practical application to the interactions in a vibration isolation system," Ph.D. Dissertation, Eindhoven University of Technology, 2011.
11. Janssen, J. L. G., J. J. H. Paulides, E. A. Lomonova, B. Delinchant, and J. P. Yonnet, "Design study on a magnetic gravity compensator with unequal magnet arrays," *Mechatronics*, Vol. 23, No. 2, 197–203, Mar. 1, 2013, doi: https://doi.org/10.1016/j.mechatronics.2012.08.003.
12. Zhou, Y., B. Kou, L. Wang, and F. Xing, "Modeling and analysis of a maglev vibration isolation unit using rectangle Halbach permanent magnet array," *2014 17th International Conference on Electrical Machines and Systems (ICEMS)*, 1711–1714, Oct. 22–25, 2014, doi: 10.1109/ICEMS.2014.7013755.
13. Zhou, Y., B. Kou, P. Liu, H. Zhang, and B. Cazzolato, "Force characteristic analysis of a magnetic gravity compensator with annular magnet array for magnetic levitation positioning system," *AIP Advances*, Vol. 8, 2018.
14. Janssen, J. L. G., J. J. H. Paulides, and E. A. Lomonova, "Study of magnetic gravity compensator topologies using an abstraction in the analytical interaction equations," *Progress In Electromagnetics Research*, Vol. 128, 75–90, 2012.
15. Zhang, Q., Y. Wang, and E. S. Kim, "Electromagnetic energy harvester with flexible coils and magnetic spring for 1–10 Hz resonance," *Journal of Microelectromechanical Systems*, Vol. 24, No. 4, 1193–1206, 2015, doi: 10.1109/JMEMS.2015.2393911.
16. Tan, Y., Y. Dong, and X. Wang, "Review of MEMS electromagnetic vibration energy harvester," *Journal of Microelectromechanical Systems*, Vol. 26, No. 1, 1–16, 2017, doi: 10.1109/JMEMS.2016.2611677.
17. Gîrtan, N. and R. Olaru, "Improving the performance of a vibration electromagnetic actuator based on active magnetic springs," *2018 International Conference and Exposition on Electrical And Power Engineering (EPE)*, 284–289, Oct. 18–19, 2018, doi: 10.1109/ICEPE.2018.8559658.
18. Woodward, M. A. and M. Sitti, "Universal custom complex magnetic spring design methodology," *IEEE Transactions on Magnetics*, Vol. 54, No. 1, 1–13, 2018, doi: 10.1109/TMAG.2017.2759099.

19. Ravaud, R., G. Lemarquand, and V, Lemarquand, "Halbach structures for permanent magnets bearings," *Progress In Electromagnetics Research M*, Vol. 14, 263–277, 2010.
20. Puccio, F. D., R. Bassani, E. Ciulli, A. Musolino, and R. Rizzo, "Permanent magnet bearings: Analysis of plane and axisymmetric V-shaped element design," *Progress In Electromagnetics Research M*, Vol. 26, 205–223, 2012.
21. Jungmayr, G., E. Marth, W. Amrhein, H. Berroth, and F. Jeske, "Analytical stiffness calculation for permanent magnetic bearings with soft magnetic materials," *IEEE Transactions on Magnetics*, Vol. 50, No. 8, 1–8, 2014, doi: 10.1109/TMAG.2014.2310437.
22. Safaeian, R. and H. Heydari, "Comprehensive comparison of different structures of passive permanent magnet bearings," *IET Electric Power Applications*, Vol. 12, No. 2, 179–187, 2018, doi: 10.1049/iet-epa.2017.0308.
23. Furlani, E. P., "Formulas for the force and torque of axial couplings," *IEEE Transactions on Magnetics*, Vol. 29, No. 5, 2295–2301, 1993, doi: 10.1109/20.231636.
24. Rakotoarison, H. L., J. Yonnet, and B. Delinchant, "Using coulombian approach for modeling scalar potential and magnetic field of a permanent magnet with radial polarization," *IEEE Transactions on Magnetics*, Vol. 43, No. 4, 1261–1264, 2007, doi: 10.1109/TMAG.2007.892316.
25. Jefimenko, O. D., *Electricity and Magnetism*, New York, Meredith Publishing Co., 1966.
26. Furlani, E. P., *Permanent Magnet and Electromechanical Devices Materials, Analysis, and Applications*, Academic Press, San Diego, 2001.
27. Rawlings, J. O., S. G. Pantula, and D. A. Dickey, *Applied Regression Analysis: A Research Tool*, 2nd Edition, Springer, 1998.
28. "Raymond, round wire compression springs, part # C1351-250-3000-S," https://www.asraymond .com/round-wire-compression-springs/C13512503000S, (accessed Dec. 22, 2020).
29. "Raymond, round wire compression springs, part # C1218-105-1000-S," https://www.asraymond .com/round-wire-compression-springs/C12181051000S, (accessed Dec. 20, 2020.